European Journal of Wood and Wood Products (2025) 83:200
https://doi.org/10.1007/s00107-025-02346-5

ORIGINAL ARTICLE

Shear capacity and slip modulus prediction of LVL and LVL-C nailed connections for LVL-I-beams

Angelo Aloisio[1] · Dag Pasquale Pasca[2] · Yuri De Santis[2] · Massimo Fragiacomo[1]

Received: 2 April 2025 / Accepted: 30 October 2025 / Published online: 5 December 2025

Abstract

Banded laminated-veneer lumber (LVL-C) is an engineered wood product valued for its high bending, tensile and compressive strength along the grain, making it well-suited for long-span, high-load members such as composite LVL I-beams. In these beams, the web is usually a unidirectional LVL, whereas the flanges are fabricated from cross-banded LVL-C to improve dimensional stability and rolling-shear resistance. This study investigates the mechanical performance of nailed LVL–LVL-C connections that link the flange to the web. Sixty push-out shear tests were carried out on eight configurations, varying (i) nail type, (ii) nail spacing (45 mm vs. 75 mm), and (iii) flange thickness (19 mm vs. 37 mm). The experiments show that flange thickness is the governing parameter: specimens with the thinner flange reached, on average, 18–20 % higher load capacity, whereas the thicker-flange specimens exhibited greater initial and secant stiffness. Two characteristic failure mechanisms were observed: single-hinge web yielding, in which one plastic hinge develops in the weak (web) member, and double-hinge composite yielding, in which a second plastic hinge forms in the strong (flange) member. These mechanisms correspond to Johansen modes (e) and (f). A nonlinear beam-on-foundation (BOF) model was developed for the nails; the model reproduces both observed failure mechanisms and the full load–slip response. Calibrating the model yields embedment strengths roughly three times the values predicted by prEN 1995-1-1, reducing the mean error in capacity prediction from 46 % to less than 1 %. A complementary linear BOF formulation confirms that the slip modulus is highly sensitive to the effective embedment depth, explaining the marked stiffness difference between the two flange thicknesses. In summary, the combined experimental–numerical programme (i) provides revised embedment parameters for spruce LVL and LVL-C, (ii) shows that current Eurocode provisions are overly conservative for these materials, and (iii) offers a validated BOF framework for designing nailed connections in LVL I-beams.

1 Introduction

Bio-based composite I-beams represent an innovative and sustainable solution for the construction industry (Dickof et al. 2014), offering high strength-to-weight ratios and improved resource efficiency (Betts et al. 2018; Fu and Sadeghian 2023; Zhang et al. 2023). These beams generally include mechanically and/or chemically bonded timber-timber composites (TTC) made from different engineered wood products (EWPs), such as Laminated Veneer Lumber (LVL)- Cross-Laminated Timber (CLT) beams and floors (Masoudnia et al. 2018), and timber I-joists with OSB webs (Kodur et al. 2017; Pelletier and Doudak 2019). In addition, hybrid systems that combine engineered wood with other materials, such as reinforced concrete or steel, have gained significant attention. Notable examples are timber-concrete composite (TCC) systems (Zhu et al. 2019; Jiang

✉ Angelo Aloisio
angelo.aloisio1@univaq.it

Dag Pasquale Pasca
dpa@treteknisk.no

Yuri De Santis
yuri.desantis@univaq.it

Massimo Fragiacomo
massimo.fragiacomo@univaq.it

[1] Department of Civil, Construction-Architectural and Environmental Engineering, Università degli Studi dell'Aquila, 67100 L'Aquila, Italy

[2] Norsk Treteknisk Institutt (Norwegian Institute of Wood Technology), Børrestuveien 3, 0373 Oslo, Norway

and Crocetti 2019) and steel-timber composite (STC) systems (Hassanieh et al. 2017; Loss and Davison 2017).

The composite action between timber joists and reinforced concrete slabs, as well as the short- and long-term behavior of TCC beams and floors, has been extensively studied through experimental investigations, analytical modeling, and finite element simulations over the past two decades (Yeoh et al. 2011; Schänzlin and Fragiacomo 2018; Khorsandnia et al. 2015; Sebastian and Cao 2024). In addition, significant efforts have been made to address the inherent limitations of timber elements, such as low stiffness, brittle tensile failure, and low shear strength, by hybridizing wood with steel or fiber-reinforced polymers (FRP) (Ghanbari Ghazijahani et al. 2017, 2015).

Typically composed of engineered wood products such as LVL, oriented strand board (OSB), or CLT, biobased composite I beams are designed to reduce environmental impact while maintaining structural performance (Chen et al. 2013). The composite I-beam web is often made of LVL or OSB, while the flanges are constructed from high-strength LVL or cross-band LVL (LVL-C), which improves dimensional stability and shear resistance (Leidorf 2019). Compared to traditional solid timber beams, bio-based I-beams are lighter, more dimensionally stable, and can span longer distances with less material usage (Dweib et al. 2006). Integrating bio-based materials also promotes using renewable resources and contributes to lower carbon emissions in construction (Gan et al. 2024). Recently, research has focused on developing innovative biobased materials with advanced microstructures (Fu and Sadeghian 2023). However, in traditional construction, the use of conventional engineered wood products is still predominant. Among them, LVL, produced from both softwood and hardwood species, is widely recognized for its superior mechanical properties in composite beam applications.

LVL is manufactured by gluing thin wood veneers (approximately 3 mm thick) with the grain running parallel to the length of the product. In some cases, LVL-C is also used. Similar to LVL, LVL-C includes cross-banded veneers, where every few veneers are oriented perpendicular to the main direction. This cross-lamination improves the dimensional stability, reduces shrinkage, and increases the shear strength perpendicular to the grain. LVL-C is particularly suitable for composite beam flanges, where the highest stresses occur.

In this work, the capacity and stiffness of LVL and LVL-C nailed connections for bio-based composite beams are examined experimentally and through analytical models. The study of nailed connections has a long history in timber connection research (Mascia and Santana 2009), as nails have traditionally been the most commonly used fasteners in structural assemblies. Most existing research has focused on nailed connections in softwood species such as Douglas fir and Norway spruce. Current research trends are exploring newly engineered wood products, especially from hardwoods and alternative softwoods (Zhang et al. 2024), and innovative nail types, including wooden nails (Wang et al. 2025).

From a modeling perspective, significant progress has been made since the 1960 s in predicting the response of timber-to-timber nailed connections. When a nailed joint is subjected to lateral loading, the resulting load-versus-interlayer-slip relationship is typically curvilinear. While some researchers have attempted to model the true curvilinear behavior (Foschi 1969; Goodman 1967; MacKay 1997; McLain 1975; Morris 1967; Mack 1977), others have simplified this relationship using various linear approximations of the actual curve. The "slip modulus" is the parameter commonly used to describe this simplified linear behavior. A method for predicting the lateral load–displacement relationship for nailed wood connections was developed from the work of McLain (1975) and (Wilkinson 1971; 1927a; 1972b; 1974a; 1974b; DeBonis and Bodig 1975). In recent years, thanks to advancements in computational power, more physics-based models have been developed, moving beyond empirical approaches. Notably, beam-on-foundation models with nonlinear embedment properties have gained traction (Pellicane et al. 1991; Zhou et al. 2009; De Santis and Fragiacomo 2021).

Despite the high fidelity of these models, the inherent variability of mechanical properties and the complexity of the non-linear behaviour of wood make the accurate prediction of nailed joint performance challenging. It is well established that the mechanical behavior of the nailed joints is influenced by several factors, including row spacing, end distance, edge distance, center-to-center spacing, and grain orientation (Blass 1994; Porteous and Kermani 2013). Furthermore, the rope effect significantly affects the overall capacity of nailed connections (Gečys et al. 2019; Rodd 1973; Sjödin et al. 2008).

The current design formulae for wood-nailed connections in structural codes are largely based on results derived from GLT and solid timber (Piazza et al. 2011; Porteous and Kermani 2013; Tomasi et al. 2010). To achieve the desired level of ductility, minimum structural requirements for nail spacing in wood connections must be met. Lau et al. (Lau 1992) provided a rational approach for understanding spacing requirements by studying wood splitting induced by nailing. Reduced nail spacing increases the risk of inducing parallel-to-grain cracks, even when no loads are applied, during the nailing process. Finally, other researchers have extensively studied the load-slip response of nailed connections, which plays a crucial role in determining the strength

and stiffness of such connections (Xu et al. 2009; Smith et al. 2011; Mascia and Santana 2009).

Regarding LVL nailed connections, many authors have focused on embedment strength (Nguyen 2020; Schweigler et al. 2016), while less attention has been paid to the behavior of the entire LVL nailed connections, particularly those involving LVL-C. For example, Wang et al. (Wang et al. 2019) studied the effect of inclined self-tapping screws connecting laminated veneer lumber on shear resistance, but this research is limited to screw connections.

To the best of the authors' knowledge, no studies have been conducted on the capacity of LVL–LVL-C nailed connections for bio-based composite beam applications.

The objectives and novelty of this work are summarized as follows. (i) Evaluate the effect of nail type, nail spacing (45 mm and 75 mm), and flange thickness (19 mm and 37 mm) on the connection capacity. (ii) Investigate whether Johansen's equations provide accurate predictions of the capacity of these connections and assess the relative prediction error. (iii) Analyze the mechanics of the connection using a nonlinear beam-on-foundation model also used to indirectly estimate the values of the embedment strengths. (iv) Compare the prediction of the slip modulus using the empirical model proposed in Eurocode 5 (EC5) with a beam-on-foundation model that assumes linear embedment properties. (v) Perform a parametric analysis of the beam-on-foundation model to assess the influence of embedment depth, nail length, and nail diameter on the predicted slip modulus. This analysis aims to propose enhancements to the empirical formulation for more accurate prediction of the slip modulus.

2 Experimental tests

The motivation for the experimental campaigns comes from the growing demand for high-performance sustainable structural solutions in modern wood construction. Bio-based composite beams, particularly those that incorporate engineered wood products such as LVL and LVL-C, offer significant advantages in terms of strength, stiffness, and environmental impact. The experimental tests aim to evaluate the effect of key parameters such as nail type, nail spacing, and flange thickness on the mechanical performance of LVL-LVL-C nailed connections.

Table 1 Main average characteristics of the LVL material used for the I-beam assembly. MC stands for Moisture Content

Commercial name	Class	Density (kg/m^3)	MC (%)
Kerto®LVL S-beam	LVL 48 P	510	12
Kerto®LVL Q-panel	LVL 36 C / 32 C	510	12

2.1 Test description

Eight test configurations were designed to represent segments of LVL–LVL-C I-beams, in which a cross-banded LVL flange is connected to a unidirectional LVL web by nails. The web is a unidirectional spruce LVL (Kerto LVL S-beam) manufactured in accordance with EN 14374; all veneers are oriented parallel to the member axis, providing high longitudinal strength and stiffness. The flange is a cross-banded LVL (Kerto LVL Q-panel) in which roughly one veneer in three is oriented perpendicular to the main grain direction. This cross-lamination increases rolling-shear strength and improves dimensional stability, making the material suitable for flanges, floor diaphragms, and wall panels. Both LVL types are produced from 3 mm rotary-peeled, strength-graded Norway-spruce (*Picea abies*) veneers bonded with a weather- and boil-resistant phenol-formaldehyde adhesive. The veneers are hot-pressed at 1.3–1.5 MPa into a continuous billet, which is subsequently sawn to the required beam, plank, or panel dimensions.

In this study, two flange thicknesses, 19 mm and 37 mm, were tested to assess their influence on the overall shear capacity and stiffness of the nailed connections. Both materials comply with EN 14374 for laminated veneer lumber and exhibit consistent mechanical properties, making them ideal for experimental analysis of load-bearing connections. Table 1 summarizes the strength grades or classifications for the KERTO products according to EN 14374.

Regarding the grading, KERTO S is classified as LVL 48 P, where 48 refers to the characteristic bending strength in the primary grain direction (48 N/mm^2). The letter P represents the orientation of the parallel grain, indicating that all veneers are aligned in the same direction to provide maximum strength along the length of the beam. The KERTO Q panel is classified as LVL 36 C / 32 C, where the characteristic strengths differ depending on the orientation of the veneer: (i) 36 C characterized by longitudinal layers with a characteristic bending strength of 36 N/mm^2; (ii) 32 C characterized by cross layers with a bending strength of 32 N/mm^2, where the letter C indicates the presence of cross-laminated layers. The samples were tested at The Norwegian Institute of Wood Technology (Norsk Treteknisk Institutt). A total of 60 samples were tested, divided into eight configurations, each consisting of 5 or 10 repetitions, as shown in Table 2.

The samples consisted of a central element made of KERTO S-beam with two side flanges made of KERTO Q-panel, each connected to the central element using two nails. The test was carried out according to NS-EN 26891 (ISO 6891), which specifies the principles for determining the strength and deformation properties of joints made with mechanical fasteners.

Table 2 Experimental matrix showing nail parameters, flange and web characteristics, and the number of repetitions. The "L/C ratio" specifies how many longitudinal (L) veneers are followed by one cross-banded (C) veneer in the flange lay-up (e.g. 2 :1 means two longitudinal veneers for every cross veneer)

Label	Nail parameters				Flange (LVL 36 C / 32 C)		Web (LVL 48 P)	Rep.
	Spacing (mm)	Producer	∅(mm)	Length (mm)	Thickness (mm)	Veneer layout (L/C ratio)	Thickness (mm)	
45-1 L	45	Bostitch	3.0	90	37	2:1	53	10
45-1 S	45	Bostitch	3.0	90	19	2:1	71	10
45-2 L	45	Senco	3.1	90	37	2:1	53	10
45-2 S	45	Senco	3.1	90	19	2:1	71	10
75-1 L	75	Bostitch	3.0	90	37	2:1	53	5
75-1 S	75	Bostitch	3.0	90	19	2:1	71	5
75-2 L	75	Senco	3.1	90	37	2:1	53	5
75-2 S	75	Senco	3.1	90	19	2:1	71	5

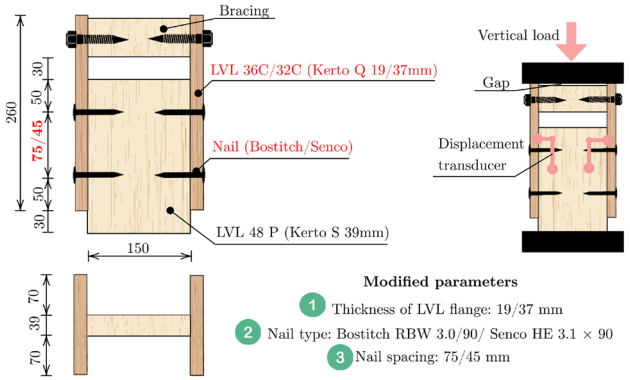

(a)

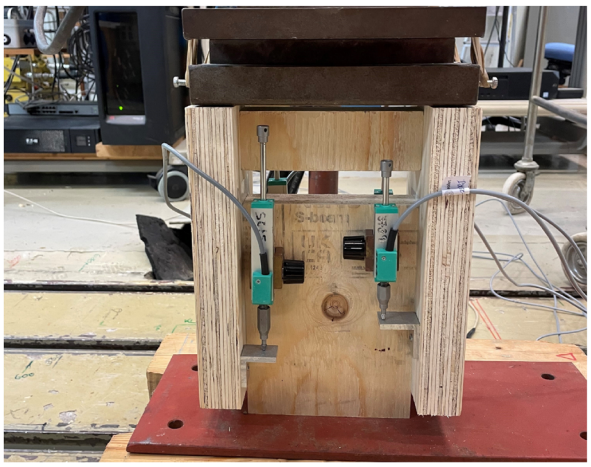

(b)

Fig. 1 **a** View of the tested configuration; **b** experimental setup

The parametric variations considered in this study were as follows: (i) Center-to-center (c/c) distance between the nails: 45 mm and 75 mm. (ii) Type of nails; Two different types of nails were tested: Bostitch RBW 3.0 / 90 and Senco HE 3.1 × 90. (iii) Flange thickness; Two thicknesses of the KERTO Q-panel were investigated: 19 mm and 37 mm. Two proprietary pneumatic nails were selected to reflect the fasteners most commonly used in the fabrication of LVL I-beams. The first is the Bostitch RBW 3.0 / 90, a 90 mm–long nail with a 3.0 mm smooth, circular shank and a full round wire head 7.0 mm in diameter. It is manufactured from bright, uncoated low-carbon steel that is cold-drawn and case-hardened, giving a bending-yield strength of approximately 1.1–1.2 GPa. The second is the Senco HE 3.1 × 90, which has the same overall length but a slightly larger shank diameter of 3.1 mm. This nail also has a smooth shank; the quenched-and-tempered steel gives a comparable yield strength of about 1.2 GPa. Under EN 1995 terminology both fasteners are classified as smooth-shank nails, since they have neither ring nor spiral threading.

To distinguish between the different configurations, the following naming system was developed: XXYZ-K. XX: The first two digits represent the center-to-center nail spacing (45 or 75 mm). Y: The third digit indicates the type of nail (1 for Bostitch and 2 for Senco). Z: The fourth letter indicates the flange thickness (S for 19 mm and L for 37 mm). K: The last digit denotes the repetition number.

Figure 1 shows (a) a view of the tested configuration and (b) the experimental setup. Two nails were inserted on each side and the relative displacement between the flange and the LVL web was measured using four LVDT sensors symmetrically placed on both faces of the sample. Four sensors were used: two with a 25-mm stroke length and two with a 50-mm stroke length.

The shear capacity of nails was the primary focus of this study, which was investigated by push-out tests. These tests involved applying a load to the central element or lateral flanges while the opposite part was held fixed. The test setup followed the principles defined in NS-EN 26891, which specifies the procedures for determining the strength and deformation properties of joints made with mechanical fasteners. The loading procedure specified by NS-EN 26891 is as follows: (i) The load was applied up to 0.4 F_{est} and held for 30 s. (ii) It was then reduced to 0.1 F_{est} and held for another 30 s. (iii) Finally, the load continuously increased until failure occurred. The test was carried out at a constant loading rate of 0.2 F_{est} per minute. The estimated Fest was

set to 5 kN, which corresponds to a loading rate of 1 kN/min.

3 Experimental results

Figure 2 shows the force-displacement curves for the eight tested configurations. Each subplot displays the overlaid curves of the 10 or 5 test repetitions for the corresponding configuration.

Table 3 summarizes the results in terms of maximum force ($F_{\max}$), displacement corresponding to 0.1 (ν_{01}) and 0.4 of $F_{\max}$ (ν_{04}), initial stiffness (k_i), secant stiffness (k_s), and ductility (D). The initial stiffness and secant stiffness were calculated as described in the appendix using Eqs. 1 and 2, respectively. The ductility was evaluated following the method outlined in the appendix in Eq. 5.

The same results presented in Table 3 are shown in graphical form as bar plots in Fig. 3.

Figure 4 illustrates the two typical failure modes observed in the nails of specimens with different flange thicknesses. It is important to note that the failure mode is influenced solely by the flange thickness and not by the nail spacing or nail type. To classify the failure mode, the authors refer to Johansen's theory. The web is identified as Member 1 (the internal and weaker element), while the flange is considered the stronger element with higher embedment strength and is designated as Member 2. In the configuration with a thicker flange (37 mm), a pronounced plastic hinge is generated in the web. The nail remains straight initially and then bends significantly at the interface, exhibiting a second curvature, albeit with a larger radius in the stronger element (flange). This results in two plastic hinges, though the hinge in the weaker element (web) is more pronounced. Consequently, this failure mode is classified as Mode (f). For specimens with a thinner flange (19 mm), the same plastic deformation is observed in the web. However, in the flange, the plastic hinge is less pronounced, with the curvature more localized and potentially occurring near the edge. This suggests a failure mode transitioning from Mode (e) to Mode (f), where the plastic hinge primarily forms in the web.

Based on these observations, the Mode (f) classification is assigned to configurations with a 37 mm flange thickness, while configurations with a 19 mm flange thickness are categorized as Mode (e-f) to reflect the transitional nature of the failure mode.

It should be remarked that the displacement plotted in Fig. 2 is the average global slips recorded by the LVDTs, i.e. the relative movement between the LVL web block and the LVL-C flange block over the entire shear plane. The LVDT-measured relative displacement is close to that of the nails.

Consequently, the predictive models adopted herein intentionally neglect geometric non-linearity: Johansen's rigid–plastic solution is formulated only for the ultimate load, and the FE beam-on-foundation model was run with small-displacement kinematics up to $F_{\max}$. At that point the measured slip remained below 3 mm (nearly 3 % of the nail

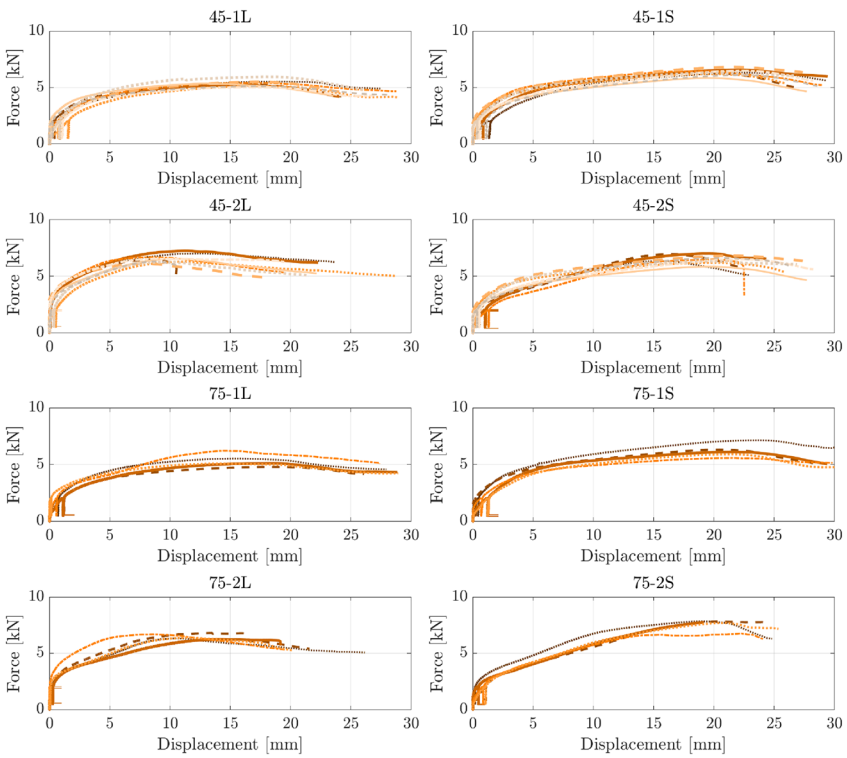

Fig. 2 Force-displacement curves of the tested eight configurations of LVL-LVLC nailed connections, as per Table2

Table 3 Main experimental results: maximum force ($F_{\max}$), displacements at 0.1 $F_{\max}$ (v_{01}) and 0.4 $F_{\max}$ (v_{04}), initial stiffness (k_i), secant stiffness (k_s) and ductility (D)

Label	$F_{\max}$ [kN]		v_{01} [mm]		v_{04} [mm]		k_i [kN/mm]		k_s [kN/mm]		D	
	Mean	CoV	Mean	CoV	Mean	CoV	Mean	CoV	Mean	CoV	Mean	CoV
45-1 L	5.4	0.1	0.5	0.3	0.6	0.3	4.5	0.3	3.4	0.3	42.1	3.5
45-1 S	6.3	0.0	0.6	0.2	0.8	0.2	3.3	0.2	2.5	0.2	43.2	9.0
45-2 L	6.5	0.1	0.1	0.4	0.2	0.4	4.0	0.4	3.7	0.4	44.4	11.7
45-2 S	6.7	0.1	0.6	0.1	0.8	0.1	3.2	0.1	2.5	0.1	45.4	11.2
75-1 L	5.2	0.1	0.6	0.2	0.8	0.2	3.7	0.3	2.8	0.3	29.1	1.6
75-1 S	6.2	0.1	0.7	0.3	0.9	0.3	3.2	0.2	2.4	0.2	27.0	1.7
75-2 L	6.4	0.0	0.2	0.2	0.3	0.2	4.3	0.2	3.0	0.2	27.8	1.7
75-2 S	7.5	0.1	0.6	0.4	0.8	0.4	3.4	0.3	2.7	0.3	24.5	1.9

Values are rounded to one decimal place; CoV = coefficient of variation

length), so second-order effects were found to be insignificant for capacity prediction.

A systematic analysis of the three main parameters, nail type, nail spacing, and flange thickness, was performed, as each parameter was varied independently while all other conditions were kept identical.

Analysis of flange thickness clearly reveals its effect on maximum load capacity ($F_{\max}$). The configurations labeled L (large) and S (small) refer to the thicknesses of the flange 37 mm and 19 mm, respectively. Reducing the thickness of the flange generally resulted in an increase in the maximum load capacity. For example, comparing configurations 45-1 L and 45-1 S, there was an 18.28% increase in capacity. A similar trend was observed for 75-1 L and 75-1 S, with an increase of 19.88%, and for 75-2 L and 75-2 S, which showed an increase of 17.00%. In contrast, the comparison between 45-2 L and 45-2 S revealed only a minor increase of 1.68%, indicating that there were no significant differences in that case. These results can be explained by focusing on the depth of embedment in the second member. Reducing the thickness of the flange increases the depth of the penetration from 53 mm to 71 mm, thus improving the connection capacity. This observation highlights the importance of the depth of the embedment also in the web in affecting the mechanical performance of nailed connections. Interestingly, the expected theoretical improvement from increasing the embedment depth on the first member was not observed experimentally, indicating a complex interaction between the two members that will be discussed in the following section. Differences in capacity due to the thickness of the flange were found to be statistically significant at 95% confidence level. A two-sample t-test confirmed that the variation in capacity was not due to random variability but rather a measurable effect of flange thickness.

In contrast to its effect on capacity, increasing the flange thickness increased both initial (k_i) and secant stiffness (k_s). The reduction in initial stiffness when the flange thickness was decreased from 37 mm to 19 mm ranged between 12.60% and 25.78%, depending on the configuration. For example, initial stiffness decreased by 25.78% for 45-1 L compared to 45-1 S and by 20.49% for 45-2 L compared to 45-2 S. Similarly, the secant stiffness decreased by values ranging from 11.37% to 33.24%, with the largest reduction observed in 45-2 L compared to 45-2 S.

Despite the observed changes in capacity and stiffness, ductility (D) did not show statistically significant differences between configurations with 37 mm and 19 mm flange thickness. However, ductility remained high across all configurations, with values ranging between 25 and 45, indicating excellent energy dissipation under cyclic loading. This ductility is primarily attributed to the behavior of the nails. Regarding the nail type, it is worth noting that Type

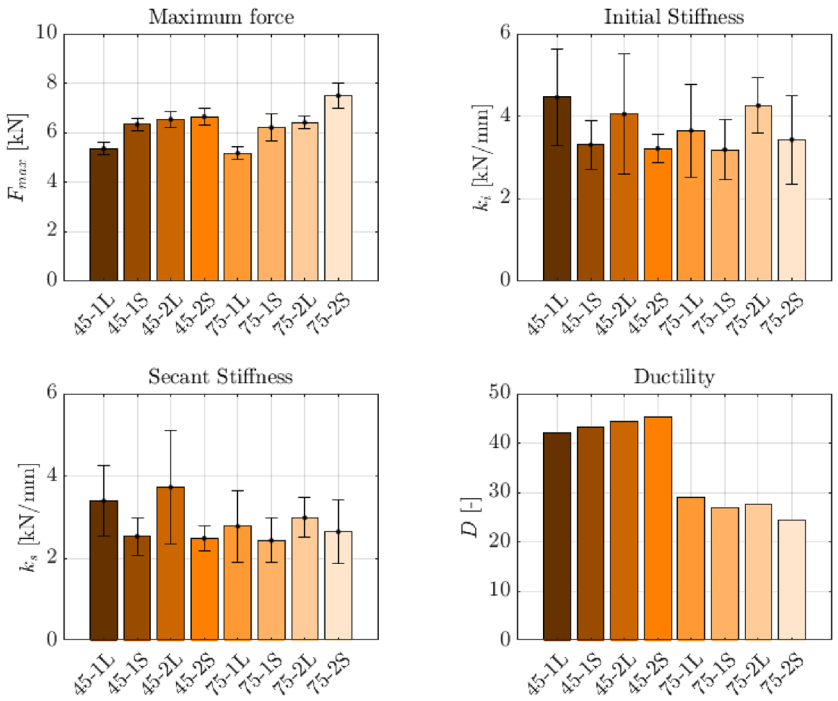

Fig. 3 Bar plot with error bar of the mean values of the maximum force, initial stiffness, secant stiffness and ductility of the 8 tested configurations in Table2

Fig. 4 View of the failure modes of the nails with the indication of the plastic hinges

1 nails have a diameter of 3 mm, while Type 2 nails are slightly larger, with a diameter of 3.1 mm. With the exception of the 45-1 S vs. 45-2 S configuration, which shows a very similar response with only a 4.89% difference in maximum capacity, the other configurations (45-1 L vs. 45-2 L, 75-1 L vs. 75-2 L, and 75-1 S vs. 75-2 S) exhibit an increase in capacity 20% to 23% due to the 0.1 mm increase in nail diameter. In terms of initial (k_i) and secant stiffness (k_s), the differences are negligible and somewhat variable. Specifically, in the configurations with 45 mm nail spacing, the 3.1 mm nails result in slightly lower stiffness values, whereas in the 75 mm spacing configurations, the same nails provide higher stiffness. However, these differences are all below 15% and should not be considered statistically significant.

As for the nail spacing, increasing the distance between nails from 45 mm to 75 mm does not produce a significant change in maximum capacity, with differences below 10% and often as little as 1%. The initial and secant stiffness are similarly unaffected. However, ductility (D) shows a more evident variation, ranging between 30% and 40%. Larger nail spacing results in a significant reduction in ductility, which is also evident in the force-displacement curves. In summary, the most notable results are as follows. At a constant nail length, increasing the thickness of the flange from 19 mm to 37 mm reduces the maximum capacity but simultaneously increases the stiffness. The nail diameter has a significant effect on capacity, with a 0.1 mm increase in diameter leading to a substantial improvement in capacity, though it does not affect stiffness. Finally, nail spacing from 45 mm to 75 mm is mainly irrelevant for capacity and stiffness, though it significantly reduces ductility.

4 Capacity prediction

4.1 Background

According to the new Eurocode 5 proposal (prEN 2020), the characteristic lateral resistance per shear plane $F_{v,d}$ of a single fastener is given by:

$$F_{\mathrm{v,k}} = F_{\mathrm{D,k}} + F_{\mathrm{rp,k}} \tag{1}$$

where $F_{D,k}$ is the characteristic dowel-effect contribution per shear plane, and $F_{\mathrm{rp,k}}$ is the characteristic rope-effect.

For timber-to-timber connections using nails, the characteristic dowel-effect contribution $F_{D,k}$ per shear plane can be derived from the Johansen equations (see Fig. 6). In the case of a symmetric connection with a fastener loaded in single shear, the characteristic dowel-effect contribution is determined by considering the four possible failure modes: (a), (b), (d), and (f), as shown in Fig. 5.

For wood-to-wood connections, factor 1.15 accounts for the differing partial safety factors, and k_{mod} for steel and wood is replaced by 1.0. Although not explicitly required by FprEN1995-1-1:2024, the factor of 1.05 is also adjusted to 1.0 for consistency and similar reasons.

$$M_{y,k} = 0.3 f_{u,k} d^{2.6} \tag{3}$$

where $f_{u,k}$ is the characteristic tensile strength of the nail.

The characteristic embedment strength $f_{h,k}$ for steel nails in structural lumber (SL), parallel laminated timber (PL), wide faces of CLT, and wide faces of LVL and GLVL is given by:

$$f_{h,k} = \frac{0.082 \rho_k d^{-0.3}}{k_{\mathrm{mat}}} \tag{4}$$

where ρ_k is the characteristic density of the embedment, d is the diameter of the nail, and $\alpha = 90°$ is the grain direction.

The material factor k_{mat} is defined as:

$$k_{\mathrm{mat}} = \begin{cases} 1.0, & \text{for SL, PL, and CL with } t_{\mathrm{layer}} > 9\,\mathrm{mm} \\ \sin^2\beta + k_1 \cos^2\beta, & \text{for softwood LVL and GLVL} \end{cases} \tag{5}$$

The factor k_1 is determined as:

$$k_1 = \begin{cases} 1, & \text{for softwood LVL-P and GLVL-P} \\ 1.2, & \text{for hardwood LVL-P and GLVL-P} \\ \frac{d}{d-2}, & d \geq 3 \quad \text{for LVL-C and GLVL-C} \\ 3, & d < 3 \quad \text{for LVL-C and GLVL-C} \end{cases} \tag{6}$$

$$F_{\mathrm{D,k}} = \min \begin{cases} f_{h,1,k}\, t_{h1}\, d & (a) \\ f_{h,2,k}\, t_{h2}\, d & (b) \\ \frac{f_{h,1,k} t_{h1} d}{1+\beta} \left[\sqrt{\beta + 2\beta^2 \left[1 + \frac{t_{h2}}{t_{h1}} + \left(\frac{t_{h2}}{t_{h1}} \right)^2 \right] + \beta^3 \left(\frac{t_{h2}}{t_{h1}} \right)^2} - \beta \left(1 + \frac{t_{h2}}{t_{h1}} \right) \right] & (c) \\ \frac{f_{h,1,k} t_{h1} d}{2+\beta} \left[\sqrt{2\beta(1+\beta) + \frac{4\beta(2+\beta) M_{y,k}}{f_{h,1,k} d t_{h1}^2}} - \beta \right] & (d) \\ \frac{f_{h,1,k} t_{h2} d}{1+2\beta} \left[\sqrt{2\beta^2(1+\beta) + \frac{4\beta(1+2\beta) M_{y,k}}{f_{h,1,k} d t_{h2}^2}} - \beta \right] & (e) \\ \sqrt{\frac{2\beta}{1+\beta}} \sqrt{2 M_{y,k} f_{h,1,k} d} & (f) \end{cases} \tag{2}$$

where $\beta = \frac{f_{h,2,k}}{f_{h,1,k}}$, $f_{h,1,k}$ and $f_{h,2,k}$ are the characteristic embedment strengths of members 1 and 2, respectively, $t_{h,1}$ and $t_{h,2}$ are the embedment depths of members 1 and 2, respectively, $M_{y,k}$ is the characteristic ultimate moment given in Eq.(3), and d is the diameter of the fastener.

The characteristic yielding bending moment for nails, according to FprEN1995-1-1:2024 (CEN 2024), is:

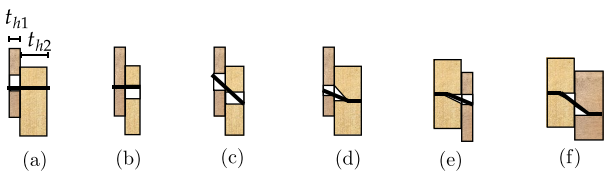

Fig. 5 Possible failure modes **a**–**f** for a fastener loaded in single shear plane

Finally, β represents the angle between the nail/staple axis and the grain direction of the wood.

Regarding the evaluation of the rope effect, the following equation is used to determine the rope-effect contribution:

$$F_{\mathrm{rp},d} = \min\left(k_{\mathrm{rp},1} F_{\mathrm{ax},t,d},\ k_{\mathrm{rp},2} F_{D,d}\right) \tag{7}$$

where, $k_{\mathrm{rp},1}$ is the factor for the rope effect, reported in Table 11.8 and equal to 0.25. $F_{\mathrm{ax},t,d}$ is the design tensile resistance. $k_{\mathrm{rp},2}$ is the limitation factor for the rope effect, as per Table 11.9. For smooth round nails and uncoated staples, it is equal to 0.15. $F_{D,k}$ is the characteristic dowel-effect contribution, determined by the following equation:

Table 4 Experimental and predicted shear capacity per single nail and shear plane estimated from Eq. 2 or (column No. 6) by optimizing the embedment strength and reducing the embedment length of the web by 28 mm, thus assuming a nail length of 62 mm for the configurations with thick flange

Label	Experimental (kN)	Predicted (kN)	Mode	Rel. Err. (%)	Predicted Opt (kN)	Mode	Rel. Err. (%)
45-1 L	1.34	0.86	f	− 36.1	1.42	d	5.7
45-1 S	1.59	0.75	e	− 52.8	1.57	e	- 0.9
45-2 L	1.64	0.93	f	− 43.3	1.53	d	- 6.2
45-2 S	1.66	0.79	e	− 52.2	1.70	e	2.1
75-1 L	1.30	0.86	f	- 33.9	1.42	d	9.4
75-1 S	1.55	0.75	e	- 51.8	1.57	e	1.2
75-2 L	1.60	0.93	f	- 42.2	1.53	d	- 4.3
75-2 S	1.88	0.79	e	- 57.6	1.70	e	- 9.5
Mean	1.57	0.83		- 46.2	1.55		- 0.3

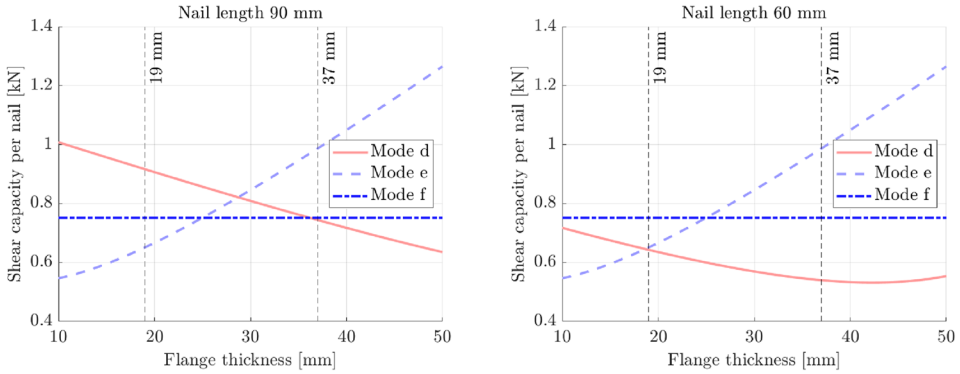

Fig. 6 Variation of the capacity associated with failure modes d, e and f considering two nail lenths

$$F_{D,k} = \sqrt{\frac{2\beta}{1+\beta}} \cdot \sqrt{2M_{y,k}f_{h,1,k}d} \cdot \min\left(\frac{t_{h1}}{t_{h1,\mathrm{req}}}, \frac{t_{h2}}{t_{h2,\mathrm{req}}}, 1\right) \tag{8}$$

The required embedment depths $t_{h1,\mathrm{req}}$ and $t_{h2,\mathrm{req}}$ are given by:

$$t_{h1,\mathrm{req}} = 2 \cdot \sqrt{\frac{M_{y,k}}{f_{h,1,k}d}} \left(\sqrt{\frac{\beta}{1+\beta}} + 1\right) \tag{9}$$

$$t_{h2,\mathrm{req}} = 2 \cdot \sqrt{\frac{M_{y,k}}{f_{h,2,k}d}} \left(\frac{1}{\sqrt{1+\beta}} + 1\right) \tag{10}$$

It should also be noted that, in order to compare the experimental results with the predictions, the safety factors were removed, and the mean values of the strengths and mechanical parameters (such as density) were used.

4.2 Results and discussion

Table 4 presents the experimental and predicted shear capacity per single nail and shear plane, estimated based on the minimum of all failure modes in Eq. 2.

Using Johansen's equations in Eq. 2, it is found that for specimens with a thicker flange (37 mm), the plastic hinge is expected to generate within the web and the flange, leading to a failure mode of type (f). Conversely, for specimens with a thinner flange (19 mm), the failure mode should be type (e), with the plastic hinge in the web. If this theoretical prediction were correct, the resistance of the specimens with the thicker flange should be slightly higher than those with the thinner flange. However, this is not observed experimentally. In fact, specimens from the S series (with thinner flanges) exhibit nearly 20% higher capacity compared to those from the L series (with thicker flanges), contrary to expectations.

To further investigate these findings, the authors conducted a parametric analysis, varying the embedment depth in both the flange and the web. In Fig. 6a, b, two different nail lengths were assumed, 90 mm and 60 mm, respectively, so that the embedment depth in the web was equal to the nail length minus the embedment depth in the flange.

It is observed that as the flange thickness increases, the capacity associated with failure mode (d) decreases. In mode (d), the plastic hinge generates in the flange (strong member, member 2), and as seen from the equation, the governing parameter is the web thickness t_1 (weak member, member 1). When the flange thickness t_2 increases, the embedment depth in the web decreases for the same nail

Table 5 Values of the embedment strength according to prEC5 and the optimized ones

Embedment strength	Estimated prEC5	Optimized	Rel. Difference
$f_{h,1}$ Web [MPa]	10.1	31.5	2.15
$f_{h,2}$ Flange [MPa]	30.2	94.5	2.15

length. Consequently, the capacity associated with mode (d) decreases as t_2 increases. On the other hand, the capacity associated with mode (f) remains largely independent of the flange thickness.

For mode (e), the capacity increases with increasing flange thickness. In mode (e), the plastic hinge arises in the web (member 1), and the flange thickness t_2 governs the capacity. Since mode (e) is proportional to t_2, increasing the flange thickness results in a higher capacity. Johansen's theory effectively predicts the failure modes: mode (e) occurs in configurations with a thin flange; mode (f) occurs in configurations with a thick flange. Furthermore, for configurations with a thick flange, mode (f) closely coincides with mode (e). This suggests that the two plastic hinges may not have fully developed simultaneously, leading to an intermediate failure mode.

Although Johansen's theory successfully identifies the failure mode, it does not fully capture two key aspects: (i) biased capacity predictions: the theoretical capacity is consistently underestimated across all configurations. (ii) unexpected higher capacity for thin-flange configurations: despite initial intuition suggesting otherwise, configurations with a thin flange exhibit higher capacity than those with a thick flange.

The first issue, i.e. systematic under-prediction of capacity was removed by a two-parameter least-squares fit where the embedment strengths of web ($f_{h,1}$) and flange ($f_{h,2}$) were treated as independent variables. The optimisation converged at $f_{h,1} = 31.5\,\text{MPa}$ and $f_{h,2} = 94.5$ MPa, i.e. 3.12 and 3.13 times the prEN 1995 values of 10.1 and 30.2 MPa (Table 5). Thus, the factor of three is not an a priori assumption but the outcome of the estimation. It happens to preserve almost exactly the code-based flange/web ratio ($f_{h,2}/f_{h,1} \approx 3$). A single multiplier, therefore, reproduces the minimum-error solution within < 1% of the two-parameter optimum. The magnitudes obtained are plausible when compared with published narrow-face tests on LVL: spruce LVL loaded with 12–16 mm dowels reported 5%, offset strengths of 30–40 MPa Franke and Quenneville (2011); Schweigler et al. (2016), while high-density beech LVL connections reached 85–95 MPa Kobel et al. (2014). Nevertheless, the present study did not include dedicated embedment tests on the narrow face of the actual LVL and LVL-C grades employed.

The second issue (higher capacity for thin-flange configurations) requires a more in-depth mechanical interpretation. LVL is significantly stiffer than other engineered wood products, leading to nail behaviour similar to a *long* beam-on-foundation model (i.e., a beam with low bending stiffness and high foundation stiffness). In this case, for mode (f) in thick-flange configurations, which can be considered a transition between mode (d) and mode (f), the plastic hinge first arises in the flange before developing in the web. Here, the web thickness t_1 governs the failure. However, if the nail behaves as a long beam, not all of its length effectively contributes to load transfer. This results in an effective nail length shorter than the actual length, reducing embedment in member 1 (web).

This behavior is illustrated in Fig. 6b, where the failure mode is (d) for thick-flange configurations and (e) for thin-flange configurations. However, the capacity of the thick-flange specimen ($t_2 = 37$ mm) is lower than that of the thin-flange specimen ($t_2 = 19$ mm), despite expectations to the contrary.

To improve capacity predictions using Johansen's theory, two modifications were introduced: (i) adjusted embedment strengths; higher embedment strength values were adopted, as reported in Table 5. (ii) Reduced embedment depth in member 1 (web); to account for the *long* beam on foundation behavior, the effective embedment depth in member 1 was reduced by 28 mm. This adjustment was applied only in thick-flange configurations to minimize the observed discrepancy in capacity between thin- and thick-flange configurations. The corrected values are summarized in Table 5.

The adjusted values agree with the experimental capacities, highlighting the following key aspects. The inherently conservative nature of current design codes and the empirical formulas for embedment strength can lead to relative errors ranging from 30% to 40% in capacity predictions. These errors can be significantly reduced by increasing the embedment strength values, which, in this study, were adjusted up to three times the original values. Moreover, LVL, being a highly rigid engineered wood product, influences the behavior of the fastener, making it behave similarly to a beam-on-foundation model in the long-beam regime. This effect is particularly relevant in failure mode (e), where the embedment in the web (t_1) governs the capacity. In this scenario, the connection behaves as if the nail were effectively shorter due to the high foundation stiffness of the LVL. As a result, in cases like the present study, a thinner flange can lead to a higher connection capacity than a thicker flange, contrary to initial expectations. This phenomenon is further supported by the parametric analysis illustrated in Fig. 6, which demonstrates the influence of the embedment depth in member 1 (web), by varying the nail length, on the predicted capacity in both flange thickness configurations.

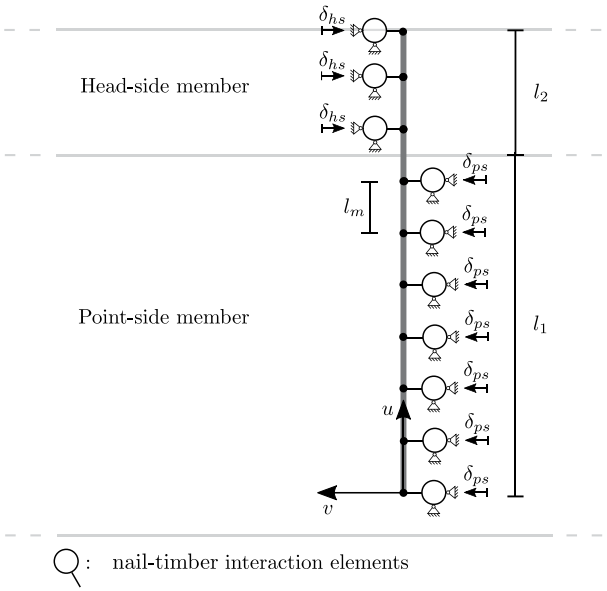

Fig. 7 Finite element models of each nail embedded in the LVL elements

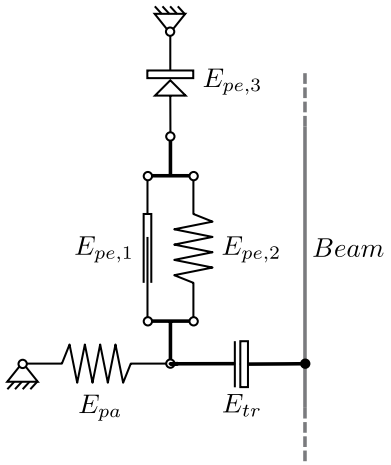

Fig. 8 Scheme of nail-timber interaction modelling

4.3 Discussion

It has been found in the previous subsection that back–calculation of the embedment strength from the push-out tests yields values of $f_{h,1}^{\exp} = 31.5$ MPa for the web and $f_{h,2}^{\exp} = 94.5$ MPa for the flange (Table 5). These values are roughly three to five times higher than the characteristic strengths predicted by the current prEN 1995-1-1 formulation for nails in softwood LVL ($\sim 10-30$ MPa). In addition, they exceed the upper range of values reported for spruce LVL in the literature (e.g. 25–45 MPa for 3-mm veneer LVL at $\rho \approx 500$ kg/m^3;(Schweigler et al. 2016, 2019)). The following points might explain this apparent discrepancy.

First of all, the tested LVL have high veneer density and hot-press consolidation. Metsä Kerto LVL and LVL-C are produced with tight veneer grading criteria and a pressing pressure of 1.3–1.5 MPa. Densification in the press raises the local density at veneer contacts well above the nominal 510 kg/m^3 used in design calculations. Because embedment strength scales almost linearly with density $\left(f_h \propto \rho^{1.0}\right)$, such local densification can easily double the effective resistance.

Additionally, in LVL-C, one veneer in three is oriented perpendicular to the main grain direction, creating a layered composite with high rolling-shear and out-of-plane compressive stiffness. Under lateral dowel loading, these cross veneers act as a restraint to lateral spreading of the fibres, increasing the confinement of the nail shank and raising the apparent embedment strength. This effect is consistent with the step-change between the web (unidirectional LVL) and the flange (cross-banded LVL-C) seen in Table 5.

Further localised densification might originate from the nail driving. The pneumatic nailers used in production introduce high strain rates ($\dot{\epsilon} \approx 10^2$ s^{-1}), which can create a densified shell immediately adjacent to the shank.

Although the experimental capacity was corrected for the rope effect using the coefficients in prEN 1995, the onset of axial load sharing can occur earlier in very stiff members. Any residual axial component increases the back-calculated f_h. Because LVL-C has a markedly higher axial stiffness than sawn timber, this mechanism is more pronounced than in previous spruce or glulam studies.

Not secondarily, the push-out arrangement places the nail in double shear with short-term, quasi-static loading. Johansen-type single-dowel embedment tests (EN 383) yield lower resistances because they measure pure compression of the fibres without additional confinement from the opposing side. Hence the current back-analysis captures a combined dowel-bearing–confinement mechanism rather than a pure embedment strength.

Still, while the high f_h values reconcile the FE predictions with the test data, they should not be transferred directly to design until validated by standard embedment tests on the same materials and nail types. The absence of such data is a limitation of the present work. Ongoing embedment tests on spruce LVL-C at NTI Oslo will help establish whether the high strengths are intrinsic material properties or artefacts of the push-out configuration. If confirmed, the high embedment strengths imply that current Eurocode procedures are overly conservative for LVL-C nailed connections, leading to unnecessarily large fastener numbers in LVL-I-beam design. Thus, a revision of the density factor or an LVL-specific k_{mat} coefficient may be justified.

4.4 Beam on foundation capacity model

The determination of the capacity of nailed connections has been simplified by modeling the nail as a beam and describing its interaction with timber using 2-node connector elements (Figs. 7 and 8).

In the finite–element formulation a beam element collapses the three-dimensional continuum into a one-dimensional problem: all field variables are functions only of the curvilinear coordinate x taken along the member axis. The kinematic assumptions depend on the beam theory adopted. In the classical Euler–Bernoulli theory a cross-section is assumed to remain plane and to rotate without in-plane distortion, so that it is both rigid and normal to the deformed axis. Timoshenko theory relaxes the "normality" condition and allows cross-sections to shear, yet still treats the section as rigid in its own plane. More sophisticated beam models (e.g. Vlasov warping, higher-order shear theories) permit limited in-plane deformation or warping, but all retain a dimensional reduction so long as the span is large compared with the cross-section dimensions. For the present nails, slender steel shanks with $l/d \approx 30$, an Euler–Bernoulli representation is sufficient; numerical tests confirmed that including shear deformation (Timoshenko) changes predicted forces and slips by less than 1 %.

The nail is modeled using one-dimensional linear beam elements, with section properties integrated into the analysis to account for the nonlinear behavior of steel. The element length, l_m, is set to one-hundredth of the overall nail length, l, ensuring sufficient discretization. An elastic–perfectly-plastic, isotropic material model is assigned to the nails. The Young's modulus is taken as $E_s = 210{,}000\,\text{MPa}$, while the yield strength is set to $f_y = 1200\,\text{MPa}$, i.e. the mid-range value reported in the manufacturers' EN 14592 datasheets (1150–1250 MPa for both the Bostitch RBW 3.0 × 90 and the Senco HE 3.1 × 90).

It should be remarked that the nail steel is modelled with an elastic–perfectly-plastic von Mises material law, the finite-element analysis already enforces the multi-axial interaction between axial force, shear and bending; no additional algebraic check of the form $N/N_{\text{pl}} + V/V_{\text{pl}} + M/M_{\text{pl}} \leq 1$ is required.

The interaction between the nail and the surrounding timber is modeled using discrete connector elements. In Abaqus/Standard (Dassault System, n.d), connector elements do not eliminate degrees of freedom; instead, kinematic constraints are enforced through Lagrange multipliers, which act as additional solution variables. Figure 8 illustrates the elementary components of the connector system used to model the complex interaction between the nail and the timber.

The element E_{pa} is an elastic–plastic spring representing the interaction along the grain direction. The timber embedment in the perpendicular direction is modeled using the analogous elastic–plastic spring $E_{pe,2}$, as illustrated in Fig. 9a and b. The elastic stiffness of each connector element, E_{pa} and $E_{pe,2}$, is defined as:

$$K_{E_{pa}} = k_h dl_m \cos\theta \tag{11}$$

$$K_{E_{pe,2}} = \beta k_h dl_m \sin\theta \tag{12}$$

where k_h represents the stiffness per unit length of the beam and is derived from Eq. 20, following the optimization of the slip modulus.

In this approach, timber is considered a fibered medium with non-interacting fibers in the two perpendicular directions. The in-plane shear stiffness within the plane of the screw is neglected, and the projection of the element length l_m over the directions parallel and perpendicular to the sliding plane defines the width of the tributary area for the connector elements, E_{pa} and $E_{pe,2}$, respectively. An elastic-perfectly plastic behavior is assumed for the connectors representing parallel-to-grain behavior (E_{pa}), while an elastic-hardening response is assumed for connectors modeling perpendicular-to-grain behavior ($E_{pe,2}$). The yielding force of E_{pa} and $E_{pe,2}$ is expressed as:

$$F_{y,E_{pa}} = f_{h,0} dl_m \cos\theta \tag{13}$$

$$F_{y,E_{pe,2}} = f_{h,90} dl_m \sin\theta \tag{14}$$

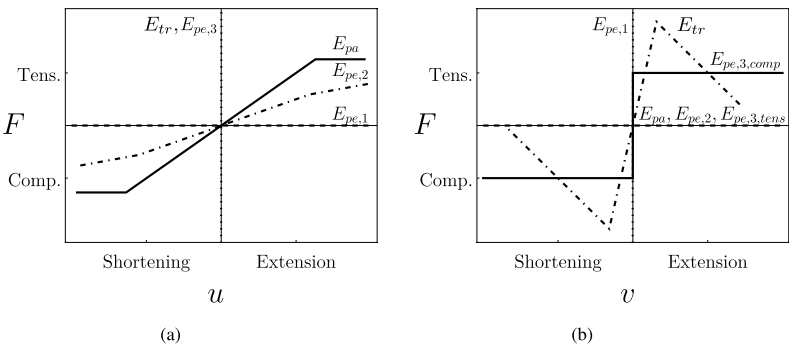

Fig. 9 Constitutive law of elements: **a** axial behaviour; **b** transversal behaviour

Table 6 Optimized finite element model parameters for each of the i-th member: embedment stiffness parallel to the sliding plane ($k_{h,i}$), embedment strength parallel to the sliding plane ($f_{h,0,i}$), embedment strength perpendicular to the sliding plane ($f_{h,90,i}$) and withdrawal strength ($f_{w,\alpha,i}$)

$k_{h,1}$ (N/mm^3)	$k_{h,2}$ (N/mm^3)	β	$f_{h,0,1}$ (N/mm^2)	$f_{h,0,2}$ (N/mm^2)	$f_{h,90,1}$ (N/mm^2)	$f_{h,90,2}$ (N/mm^2)	$f_{w,\alpha,1}$ (N/mm^3)	$f_{w,\alpha,2}$ (N/nm^3)
195,00	396,00	0,50	52,00	153,00	35,84	107,53	10,08	10,08

Table 7 Finite Element (FE) prediction of the connection capacity per single nail, assuming the embedment strength (f_h) from prEC5 as listed in Table5 and the optimized values reported in the same table

*Label	Exp. (kN)	FEM (f_h prEC5)		FE (f_h Optim. from Johansen)		FE (f_h Optim. from FE)	
		Value (kN)	Rel. Error (%)	Value (kN)	Rel. Error (%)	Value (kN)	Rel. Error (%)
45-1 L	1.34	0.69	− 48.60	1.22	− 9.24	1.49	11.19
45-1 S	1.59	0.63	− 60.51	1.21	− 23.48	1.54	− 2.85
45-2 L	1.64	0.73	− 55.05	1.30	− 20.56	1.64	0.45
45-2 S	1.66	0.66	− 60.48	1.30	− 22.08	1.65	− 0.98
75-1 L	1.30	0.69	− 46.81	1.22	− 6.09	1.54	18.63
75-1 S	1.55	0.63	− 59.69	1.21	− 21.88	1.54	− 0.82
75-2 L	1.60	0.73	− 54.14	1.30	− 18.95	1.64	2.48
75-2 S	1.88	0.66	− 64.96	1.30	− 30.91	1.65	− 12.20
Mean	1.57	0.68	− 56.28	1.26	− 19.15	1.59	1.99

The authors also used the f_h optimized from the FE model equal to 52 and 153 MPa for the web and flange, respectively. The stiffness of each member has been determined based on the calibration presented in the following section, using the values in Eq. 20

The ultimate force in the direction perpendicular to the grain at a displacement equal to $2d$ is given by:

$$F_{u,E_{pe,2}} = \Gamma F_{y,E_{pe,2}} \tag{15}$$

where Γ is taken as 1.72, based on findings by Schweigler et al. (Schweigler et al. 2016, 2019). The embedment strength parameters for E_{pa} and $E_{pe,2}$ follow the Eurocode 5 proposal and are defined in Eq. 4. The bilinear material model adopted for both E_{pa} and $E_{pe,2}$ is illustrated in Fig. 9a and b.

The friction in the shear plane is accounted for through the combination of $E_{pe,1}$ and $E_{pe,3}$. The element $E_{pe,1}$ acts as a transversely rigid but axially free component, as illustrated in Fig. 9a and b. Its primary role is to transfer forces parallel to the sliding plane between the timber and the nail. The element $E_{pe,3}$ represents a friction component, providing a reaction force parallel to the sliding plane, which is proportional to the force acting perpendicular to it, following the relationship:

$$F_{\parallel} = \mu F_{\perp} \tag{16}$$

where the friction force is only activated when the element is axially compressed.

Eurocode 5 limits the rope-effect contribution of dowel-type fasteners to $\mu_{\mathrm{EC5}} = 0.25$ (timber–timber contact, EN 1995-1-1, §11.1.2), a deliberately conservative value that safeguards long-term performance and service-class uncertainty. For the present FE simulations the authors adopted the mean static friction coefficient $\mu = 0.48$ reported by Aurand and Blaß Aurand and Blaß (2021) from a meta-analysis. This higher value reflects short-term behaviour under dry laboratory conditions and is consistent with modern guidance for engineered timber: the Finnish design guide RIL 205-1:2017 assigns $\mu = 0.40$ to LVL-to-LVL contacts, and the LVL Handbook Europe (2020) recommends the same value for face-to-face LVL interfaces. Using $\mu = 0.48$ therefore captures the experimentally observed slip stiffness without compromising the code-based safety design.

The withdrawal behavior of the screw is modeled through rigid-plastic connectors denoted as E_{tr}, whose properties are defined according to the new Eurocode 5 proposal. The withdrawal failure force per connector is given by:

$$F_{u,E_{tr}} = f_{w,\alpha}\pi d l_m \tag{17}$$

To simulate withdrawal failure, a linear damage evolution model is assigned to E_{tr}. Based on the detailed three-dimensional finite element analyses conducted by Bedon et al. (Bedon and Fragiacomo 2019), an ultimate displacement of $4\,\mathrm{mm}$ is assumed for the damage evolution. Regarding the boundary conditions, the head-end of the screw is considered free, as depicted in Fig. 7.

Table 7 presents the predictions of the finite element (FE) model described earlier, using three sets of embedment strength values. The first set corresponds to the predictions from the prEC5 formulation, while the second set consists of the optimized values reported in Table 5. The third set of f_h values was optimized using the FE model, resulting in 52 MPa for the web and 153 MPa for the flange, respectively (Table 6).

The stiffness of each member has been determined through calibration, as described in the following section, using the values provided in Eq. 20.

Assuming the embedment strength f_h from prEC5, the predicted capacity exhibits an average underestimation error of 56%, which aligns with the 46% underestimation observed using Johansen's equations. This consistency reinforces the validity of Johansen's theory for such connections. By increasing the embedment strength to the optimized values reported in Table 5, the error reduces to approximately 20%. This clearly indicates that the embedment strength predicted by prEC5 significantly underestimates the actual values for the LVL specimens considered. However, due to the lack of dedicated embedment strength experimental tests, direct verification was not possible. The embedment strength values obtained by optimizing the FE model are even higher than those derived from the Johansen-based optimization and approximately five times greater than those estimated using prEC5. This unequivocally confirms that the prEC5 predictions significantly underestimate the embedment strength.

Moreover, as previously observed with Johansen's equations, the FE model predicts a lower capacity for the configuration with a thicker flange compared to the one with a thinner flange, whereas experimental results show the opposite trend. Nevertheless, it is noteworthy that increasing the embedment strength significantly reduces the discrepancy between these two configurations. Specifically, the difference in predicted capacities decreases from an average of 10% when using f_h from prEC5 to less than 1% when adopting the optimized embedment strength. Further increasing f_h results in a slight trend inversion, with the L samples exhibiting lower resistance than the S samples, as observed experimentally.

Figure 10 displays the longitudinal stress in the nail at the bottom, centroid, and top fiber for the configurations **a** 45-1 L and **b** 45-1 S.

Figure 10 confirms the experimental observations from Fig. 4. In the configuration with a thick flange, two distinct plastic hinges develop (one in each member) matching the experimental findings. Conversely, in the case of a thinner flange, the plastic hinge in the web is clearly visible, while the one in the flange is less pronounced, appearing only marginally. This confirms that the failure mode is a transitional case between modes (e) and (f) according to Johansen's classification. The outer fibres locally reach $\sigma_{11} \simeq 1.1$ GPa, a value compatible with the adopted yield strength of 1.2 GPa for cold-worked carbon-steel nails (EN 14592).

Figure 11 presents the axial shear force, bending moment, longitudinal and transverse displacements in the nails, along with the corresponding force-displacement curve. The plots illustrate the evolution of each curve, with shading representing the transition from the least loaded (lighter) to the most loaded (darker) condition. The two tiled plots correspond to the (a) 45-1 L and (b) 45-1 S configurations.

The figure not only illustrates the shear mechanical behavior of the connection but also highlights distinct differences between the connections with thick and thin flanges, particularly in terms of shear distribution. In the configuration with a thick flange, the shear force is significant along the entire nail length within the web. In contrast, for the thin flange configuration, shear is absent over an initial length of approximately 30 mm. This observation aligns with the optimization results presented in Table 4, where the effective web thickness was found to be 43 mm. This behavior is attributed to the high stiffness of LVL, which causes the nail to behave as a beam on an elastic foundation with characteristics of a long beam.

Figure 12 illustrates the evolution of stress parallel to the grain in the wood as a function of the vertical displacement (δ) of one member and the position along the nail length.

In both cases, (a) corresponding to the 45-1 L configuration and (b) to the 45-1 S one, differences in the extent and position of the plasticized zone on the wood side can be observed. In Fig. 12a, for the L configuration, the stresses

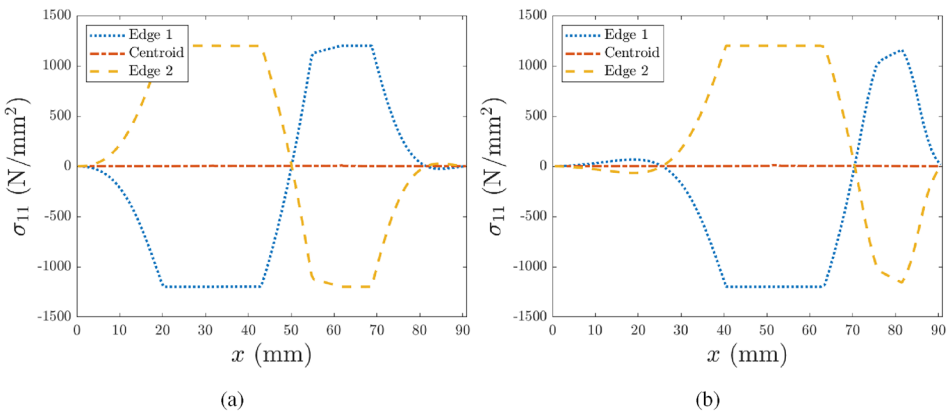

Fig. 10 Longitudinal stress (σ_{11}) in the nail at the bottom, centroid, and top fiber for the configurations: **a** 45-1 L and **b** 45-1 S

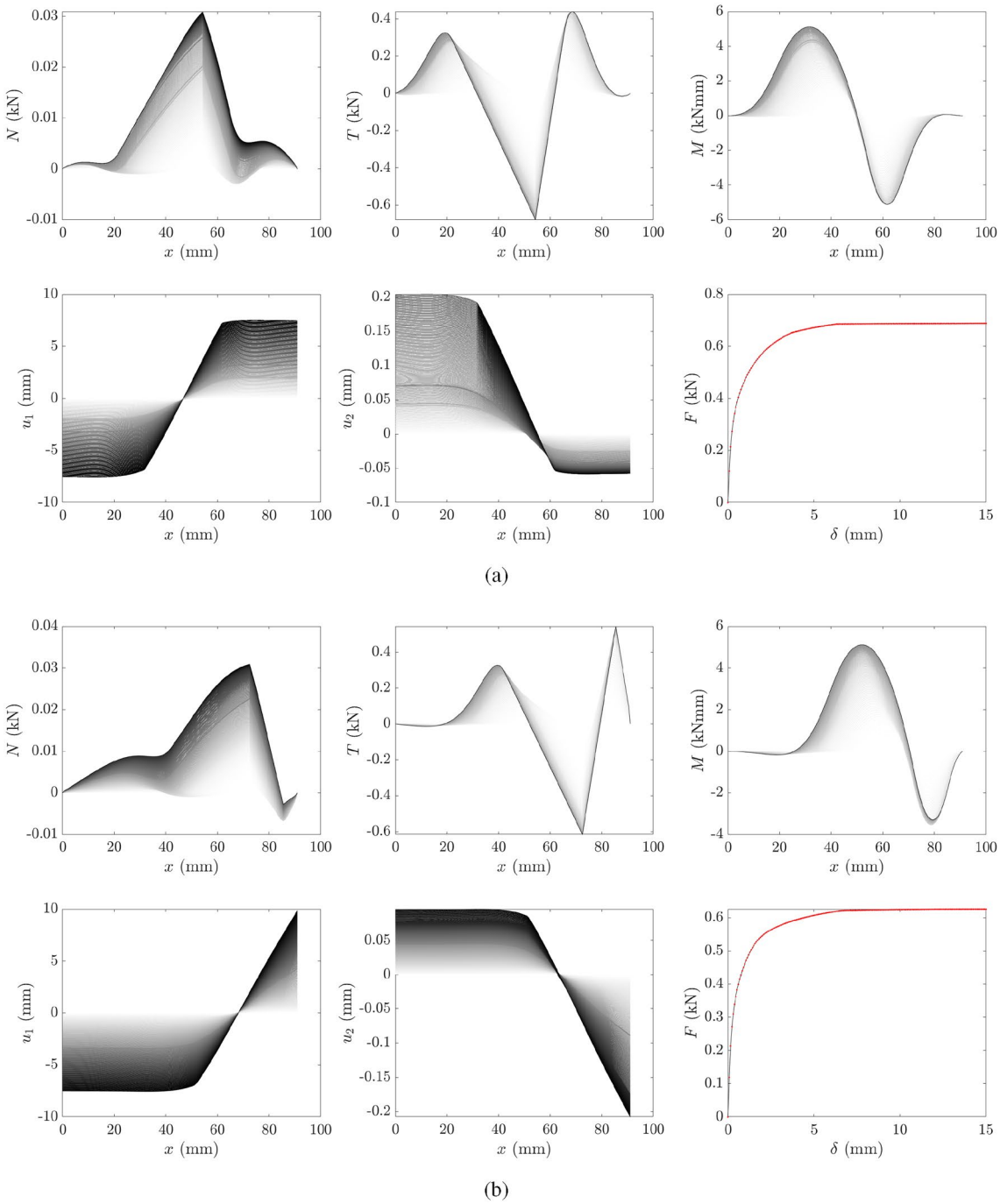

Fig. 11 Axial (N) shear (T) force, (M) bending moment, longitudinal (u_1) and transverse (u_2) displacements in the nails, and the corresponding force (F)-displacement (δ) curve. The plots illustrate the evolution of each curve, with shading indicating the transition from the least loaded (lighter) to the most loaded (darker) condition. The tiled plots correspond to: **a** 45-1 L and **b** 45-1 S configurations: **a** 45-1 L and **b** 45-1 S

reach their peak and then gradually decrease beyond 70 mm. Conversely, in Fig. 12b, for the S configuration, the stresses reach their maximum at 70 mm and remain at this peak level up to the nail's end, indicating that nearly the entire flange is plasticized.

5 Slip modulus prediction

The full non-linear BOF model reproduces the complete load–slip response; however, a single simulation requires approximately 40 min of CPU time. To perform the extensive slip-modulus parametric study, the authors therefore

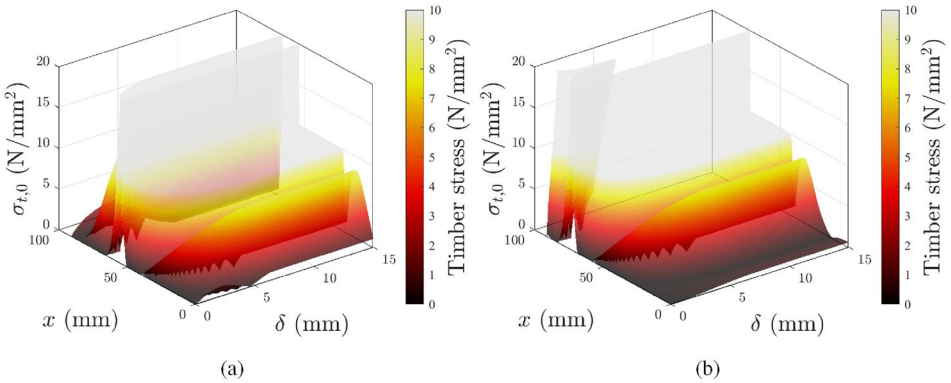

Fig. 12 Evolution of the tensile stress parallel to the grain on the wood side ($\sigma_{t,0}$) as a function of the vertical displacement (δ) of one member and the position along the nail length (x). **a** corresponds to the 45-1 L configuration, while **b** to the 45-1 S configuration

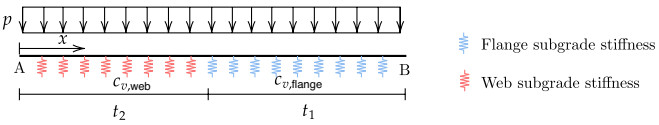

Fig. 13 Beam on foundation model of the nail on two subgrade segments, the web and the flange

Table 8 Experimental vs predicted slip modulus according to Eq. 18

Label	Experimental (kN/mm)	EC5 Predicted (kN/mm)	Rel Err. (%)	BOF Predicted (kN/mm)	Rel Err. (%)
45-1 L	0,85	0,92	8,8%	0,70	−17,3%
45-1 S	0,64	0,92	45,6%	0,66	4,5%
45-2 L	0,93	0,95	1,8%	0,74	−21,0%
45-2 S	0,62	0,95	52,5%	0,69	10,9%
75-1 L	0,70	0,92	33,0%	0,70	1,2%
75-1 S	0,61	0,92	51,6%	0,66	8,8%
75-2 L	0,75	0,95	27,0%	0,74	− 1,4%
75-2 S	0,66	0,95	43,3%	0,69	4,2%
Mean	0,72	0,94	32,9%	0,70	− 1,2%

introduced a lightweight linear BOF surrogate: the nail is idealised as an Euler–Bernoulli beam resting on two elastic foundations, whose values are first calibrated from the non-linear model. Because this closed-form solution evaluates in milliseconds, it is well suited to large parameter sweeps; the analytical derivation is presented in the following paragraphs.

5.1 Methods

According to the new Eurocode 5 proposal, the slip modulus of timber-to-timber nail connections per shear plane can be calculated as follows:

$$K_{\text{SLS},v,i} = \frac{\rho_{\text{mean}}^{1.5} \cdot d^{0.8}}{30} \tag{18}$$

where ρ_{mean} is the mean density of the two members, which in this case is equal to 510 kg/m^3, and d is the nail diameter.

A reduced-order model was also developed to predict the slip modulus based on a linear beam-on-foundation (BOF) approach, where both the beam (nail) and the embedment are assumed to behave linearly, see Fig. 13. The fundamental assumption in beam theory is the indeformability of the cross-section. Since the nail has a solid circular cross-section, it belongs to the category of compact sections, which are not prone to in-plane section deformation. This validates the fundamental assumption of beam theory, ensuring an accurate representation of the nail's mechanical response. The beam elements used to model the nail are treated as one-dimensional linear elements, with section properties integrated into the analysis to account for the steel's non-linear behavior. Following the approach in (De Santis and Fragiacomo 2021), two coupled differential equations were solved to model the response of the metal fastener embedded in timber.

An elastic isotropic behavior was assumed for the nail steel, with a Young's modulus of $E_s = 210000\,\text{N/mm}^2$. The interaction between the nail and the surrounding timber was modeled using a linear embedment stiffness, c_v, which was estimated by solving the following optimization problem:

$$\{\hat{c}_{v,\text{flange}}, \hat{c}_{v,\text{web}}\} = \arg\min_{c_v} \sum_{i=1}^{n} \left(K_{\text{SLS},v,i,\text{exp}} - K_{\text{SLS},v,i,\text{BOF}}\right)^2 \tag{19}$$

where $K_{\text{SLS},v,i,\text{exp}}$ and $K_{\text{SLS},v,i,\text{BOF}}$ represent the experimental slip modulus and the slip modulus obtained from the beam-on-foundation (BOF) model, respectively. The parameters $\hat{c}_{v,\text{flange}}$ and $\hat{c}_{v,\text{web}}$ correspond to the optimized embedment stiffness of the flange and web members, respectively.

This approach allows for a systematic estimation of the embedment stiffness in both flange and web elements, improving the predictive capability of the model in evaluating the slip modulus of LVL-LVL-C nailed connections.

5.2 Results

Table 8 compares the experimental and predicted slip modulus according to Eq. 18. It is observed that the empirical formula provides an accurate prediction for the L-series with a larger flange thickness. However, it significantly overestimates the slip modulus for the S-series with a smaller flange thickness, with an error ranging from 40% to 50%. This highlights that for LVL and LVL-C materials, unlike other engineered wood products such as Glulam or CLT, the embedment depth is a critical parameter in estimating stiffness.

The embedment stiffness of the internal member, referred to as the web, and the external member, referred to as the flange, were estimated by solving the optimization problem presented in Eq. 19. The obtained values are:

$$\{\hat{c}_{v,\text{flange}}, \hat{c}_{v,\text{web}}\} = \{396\ \text{N/mm}^2, 195\ \text{N/mm}^2\} \tag{20}$$

It is noteworthy that the embedment stiffness of the LVL-C flange is approximately twice that of the LVL web. This highlights the significant role played by both the fiber orientation relative to the nail and the presence of cross-laminated layers in LVL-C, which enhance stiffness and mechanical performance.

Table 8 presents the slip modulus predictions obtained using the values in Eq. 20. Since the optimization problem was formulated to minimize the global error across all configurations, the relative mean error is nearly negligible. Additionally, the results confirm the experimental observations, indicating that flange thickness is a determining factor in stiffness. A thinner flange leads to a significantly lower slip modulus.

Although the BOF model successfully captures this trend, experimental data show a more pronounced difference between the configurations with narrow and wide flanges. A univariate parametric analysis was performed to further evaluate the contribution of different parameters to the slip modulus. This analysis involved varying individual parameters while keeping all others constant. The model parameters corresponding to the experimental configuration 45-1 L were used as a reference.

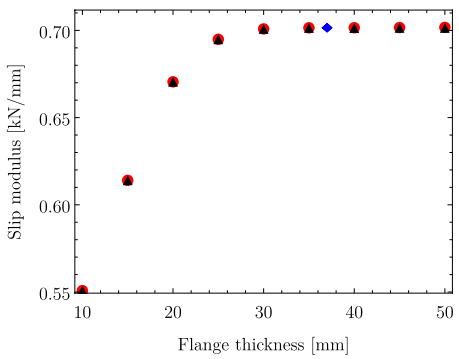

Fig. 14 Variation of the slip modulus with flange thickness: constant length of embedment in the central member (red dot), constant nail length (black triangle), first experimental configuration (blue diamond)

Specifically, in the first study, the flange thickness was varied while maintaining a constant nail embedment length in the central member (53 mm), which consequently altered the overall nail length (red dots in Fig. 14). In the second study, the flange thickness was again varied, but this time with a constant nail length of 90 mm, thereby modifying the nail embedment length in the central member (black triangles in Fig. 14).

This approach enabled a systematic assessment of the influence of embedment depth and flange properties on the slip modulus. More specifically, it allowed us to determine whether the variation in slip modulus was solely due to changes in flange thickness or rather a result of variations in embedment length in the central member or overall nail length.

The results of both parametric analyses in Fig. 14 yielded consistent outcomes, indicating that the slip modulus variation is primarily governed by changes in flange thickness rather than by variations in either the embedment length in the central member or the overall nail length. The variability in the slip modulus ranges from approximately 0.55 to 0.7, showing an almost linear increase as the flange thickness increases from 10 mm to 30 mm.

Beyond a thickness of 30 mm, the slip modulus stabilizes and remains nearly constant. This suggests that increasing the flange thickness beyond this point does not provide a more effective clamping effect for the nails than that achieved with a flange of approximately 30 mm. Consequently, further increases in flange thickness do not significantly enhance the connection stiffness.

6 Conclusion

This study presents the results of an experimental campaign on 60 LVL and LVL-C nailed connections. These connections replicate the interface between the flange and web in LVL composite I-beams, where the flange is made of LVL-C and the web of LVL.

Eight configurations were tested to analyze the influence of three key parameters: nail type, nail spacing, and flange thickness. The results indicate that reducing the flange thickness unexpectedly increased the maximum load capacity by

approximately 20%. According to Johansen's theory, configurations with different flange thicknesses should exhibit different failure modes: mode *e* for thicker flanges and mode *d* for thinner flanges. Theoretically, the thicker flange should result in a higher load capacity. However, the experimental results showed that even in the thinner flange configurations, failure occurred in mode *e*, with plastic hinge formation in the outermost member (Member No.1). This resulted in a higher load capacity for the configurations with a thinner flange. The reason for this behavior lies in the properties of LVL-C, which provide sufficient clamping action, ensuring plastic hinge formation in the outer member despite its reduced thickness.

The experimental findings reveal the interplay between flange thickness, nail type, and nail spacing in LVL-LVL-C nailed connections. While reducing the flange thickness led to a increase in load capacity, it also resulted in a decrease in both initial (k_i) and secant stiffness (k_s). The reduction in stiffness ranged from 12.60% to 25.78%, depending on the configuration. Despite these variations in capacity and stiffness, ductility (D) remained largely unaffected, indicating that the connections maintained their ability to undergo inelastic deformation regardless of flange thickness.

The nail type also played a crucial role in determining capacity. Although the difference in diameter between the two nail types was minimal (3 mm vs. 3.1 mm), the impact on load-bearing capacity was substantial. With the exception of the 45-1 S vs. 45-2 S configuration, where the difference was negligible (4.89%), all other comparisons (45-1 L vs. 45-2 L, 75-1 L vs. 75-2 L, and 75-1 S vs. 75-2 S) exhibited a 20% to 23% increase in capacity with the slightly larger nail diameter. Conversely, nail spacing had little effect on the connection performance. Increasing the spacing from 45 mm to 75 mm resulted in differences in maximum capacity below 10%, and in many cases, as little as 1%. This indicates that within the tested range, nail spacing is not a governing factor in determining load-bearing capacity, although it may still influence failure modes and long-term performance.

The experimental results reveal that Johansen's theory correctly predicts the governing failure modes but underestimates the shear capacity, with errors exceeding 40% for certain configurations. The unexpected higher capacity of thin-flange configurations is attributed to the nail behaving as a long beam-on-foundation, reducing the effective embedment depth in the web for thick-flange configurations. By optimizing the embedment strength and accounting for reduced embedment depth, the predictive accuracy was significantly improved, aligning more closely with experimental values.

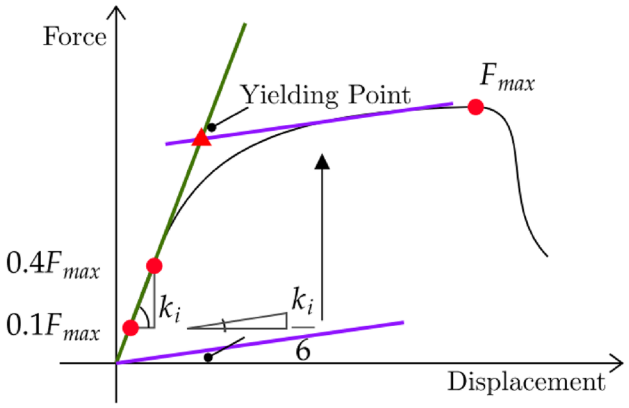

Fig. 15 Illustration of the yielding point estimation

Stiffness and ductility estimation

Stiffness estimation

The force displacement and moment rotation were used to determine the stiffness of the connection at each stage of the test. The initial slip modulus, which indicates the stiffness of the connection during the first loading phase, is calculated using the following definition:

$$k_i = \frac{0.4F_{est}}{\nu_{04}} \tag{1}$$

Where F_{est} is the estimated maximum load and ν_{04} is the connection displacement at $0.4F_{est}$. The slip modulus measures the stiffness of the connection in the first loading phase, neglecting the initial slip, and it is determined with the following definition:

$$k_s = \frac{0.4F_{est} - 0.1F_{est}}{\nu_{04} - \nu_{01}} \tag{2}$$

ν_{04} and ν_{01} are the relative slips in the loading phase corresponding to $0.4F_{est}$ and $0.1F_{est}$ respectively. The ultimate slip modulus as defined in the Eurocode 5 Eurocode (2004) is:

$$k_u = \frac{2}{3}k_s \tag{3}$$

However, the commonly used reduction factor of 2/3 may not accurately capture the true behavior of different joint types, potentially resulting in an inaccurate estimation of ultimate stiffness Jockwer and Caprio (2021). To consider the actual non-linear load–displacement behavior of connections at the ultimate limit state a different approach to estimating the effective stiffness near failure, based on

experimental data, was proposed in De Santis et al. (2024) and subsequently applied here:

$$k_{u,p} = \frac{F_{max} - 0.6F_{max}}{\nu_u - \nu_{06}} \tag{4}$$

Where ν_u and ν_{06} are the relative slip in the reloading phase corresponding to F_{max} and $0.6F_{max}$.

Ductility estimation

Ductility can be defined as the ability of the joint to undergo large amplitude slip in the plastic range without a substantial reduction of strength. It can be measured as the ratio between ultimate slip u_u and yield slip u_yEN (2005).

$$D = \frac{u_u}{u_y} \tag{5}$$

Although this definition was originally intended for assessing ductility through cyclic tests, it can still provide a qualitative evaluation of the expected ductility for different connection types. According to EN (2005) the yield slip is determined by the intersection of the following two lines, as shown in Fig. 15:

- The secant line passing through the point on the load-slip curve corresponding to $0.1F_{\max}$ and the point on the load-slip curve corresponding to $0.4F_{\max}$;
- The tangent line to the experimental curve, obtained by translating upward a line with a slope equal to $1/6$ of the first line's slope.The ultimate slip u_u as for EN 12512 EN (2005) is taken as the minimum of 30 mm, and the slip corresponding to a 20% load reduction concerning the maximum force achieved during the test.

Acknowledgements The authors thank Lett-Tak Systemer AS for the fabrication of the tested specimens.

Author contributions All the authors equally contributed to this research

Funding Open access funding provided by Università degli Studi dell'Aquila within the CRUI-CARE Agreement.

Data availability No datasets were generated or analysed during the current study.

Declarations

Conflict of interest The authors declare no Conflict of interest.

References

Aurand S, Blaß HJ (2021) Connections with inclined screws and increased shear plane friction. Proceedings - meeting 54 : 16-19 August 2021, online meeting / inter, international network on timber engineering research. In: Görlacher R (ed.) (p 147-168)

Bedon C, Fragiacomo M (2019) Numerical analysis of timber-to-timber joints and composite beams with inclined self-tapping screws. Compos Struct 207:13–28. Retrieved from https://doi.org/10.1016/j.compstruct.2018.09.008

Betts D, Sadeghian P, Fam A (2018) Experimental behavior and design-oriented analysis of sandwich beams with bio-based composite facings and foam cores. J Compos Constr 22(4):04018020

Blass H (1994) Variation of load-slip behavior in nailed joints: variation parallel to the grain. For Prod J 44(1):15

CEN (2024). Fpren 1995 eurocode 5: design of timber structures (Vol 1)

Chen A, Davalos J, Jiao P, McGraw B (2013) Buckling behavior of sinusoidal web for composite wood i-joist with elastically restrained loaded edges under compression. J Eng Mech 139(8):1065–1072. https://doi.org/10.1061/(ASCE)EM.1943-7889.0000443

Dassault Systèmes (n.d.). Abaqus

De Santis Y, Aloisio A, Pasca DP, Gavri I, Fragiacomo M (2024) Mechanical characterization of soundproofed inclined screws connections. Constr Build Mater 412:134641

DeBonis AL, Bodig J (1975) Nailed wood joints under combined load. Wood Sci Tech nol 9(2):129–144

De Santis Y, Fragiacomo M (2021) Timber-to-timber and steel-to-timber screw connections: derivation of the slip modulus via beam on elastic foundation model. Eng Struct 244:112798

Dickof C, Stiemer S, Bezabeh M, Tesfamariam S (2014) Clt-steel hybrid system: ductility and overstrength values based on static pushover analysis. J Perform Constr Facil 28(6):A4014012. https://doi.org/10.1061/(ASCE)CF.1943-5509.0000614

Dweib M, Hu B, Shenton Iii H, Wool R (2006) Bio-based composite roof structure: manufacturing and processing issues. Compos Struct 74(4):379–388

EN 12512:2001 + A1:2005 (2005) Timber structures—test methods—cyclic testing of joints made with mechanical fasteners. 3(1)

Eurocode-5 (2004) Design of timber structures—Part 1-1: General—Common rules and rules for buildings. CEN

Foschi RO (1969) The load-slip characteristics of nails. Canadian Forestry Service, Western Forest Products Lab, Vancouver, British Columbia

Franke S, Quenneville P (2011) Bolted and dowelled connections in radiata pine and IVI using the European yield model. Aust J Struct Eng 12(1):13–27. https://doi.org/10.1080/13287982.2011.11465018

Fu Y, Sadeghian P (2023) Bio-based sandwich beamsmade of paper honeycomb cores and flax frp facings: flexural and shear characteristics. Structures (Vol 54, pp 446–460)

Gan Z, Sun Y, Li Z, He M (2024) Experimental and numerical investigation on the in-plane performance of nail-laminated timber floor. J Build Eng 96:110509
Gečys T, Bader TK, Olsson A, Kajeėnas S (2019) Influence of the rope effect on the slip curve of laterally loaded, nailed and screwed timber-to-timber connections. Constr Build Mater 228:116702
Ghanbari Ghazijahani T, Jiao H, Holloway D (2015) Rectangular steel tubes with timber infill and cfrp confinement under compression: experiments. J Constr Steel Res 114:196–203. https://doi.org/10.1016/j.jcsr.2015.07.015
Ghanbari Ghazijahani T, Jiao H, Holloway D (2017) Composite timber beams strengthened by steel and cfrp. J Compos Constr 21(1):04016059. https://doi.org/10.1061/(ASCE)CC.1943-5614.0000714
Goodman JR (1967) Layered wood systems with interlayer slip (Unpublished doctoral dissertation). University of California, Berkeley
Hassanieh A, Valipour H, Bradford M (2017) Composite connections between clt slab and steel beam: experiments and empirical models. J Constr Steel Res 138:823–836. https://doi.org/10.1016/j.jcsr.2017.09.002
Jiang Y, Crocetti R (2019) Clt-concrete composite floors with notched shear connectors. Constr Build Mater 195:127–139. https://doi.org/10.1016/j.conbuildmat.2018.11.066
Jockwer R, Caprio D (2021) Reliability of complex timber structures: impact of connection non-linearity and overstrength. 14th international conference on applications of statistics and probability in civil engineering(icasp14). Retrieved from http://hdl.handle.net/2262/103574
Khorsandnia N, Schanzlin J, Valipour H, Crews K (2015) Coupled finite element-finite difference formulation for long-term analysis of timber-concrete composite structures. Eng Struct 96:139–152. https://doi.org/10.1016/j.engstruct.2015.03.047
Kobel P, Frangi A, Steiger R (2014) Dowel-type connections in lvl made of beechwood. Proc., international network on timber engineering (inter)meeting (Vol 47)
Kodur V, Stein J, Fike R, Tabbador M (2017) Comparative fire performance of traditional lumber and engineered wood joists. J Struct Fire Eng 8(1):2–13
Lau PW (1992) Rationalizing spacing requirements for nailed wood connections by induced wood splitting. Can J Civ Eng 19(5):842–846
Leidorf M (2019) Lvl handbook. Leidorf Publications. Retrieved from https://www.leidorf.com/wp-content/uploads/2019/10/lvl-handbook.pdf
Loss C, Davison B (2017) Innovative composite steel-timber floors with prefabricated modular components. Eng Struct 132:695–713. https://doi.org/10.1016/j.engstruct.2016.11.062
Mack JJ (1977) The load-displacement curve for nailed joints. J Inst Wood Sci 7(6):34–36
MacKay RB (1997) Timber frame tension joinery. University of Wyoming
Mascia NT, Santana CLDO (2009) Remarks on the slip modulus of nailed connections for linear analysis of plywood timber beams. Constr Build Mater 23(8):2731–2737
Masoudnia R, Hashemi A, Quenneville P (2018) Predicting the effective flange width of a CLT slab in timber composite beams. J Struct Eng (United States) 144(7):04018084. https://doi.org/10.1061/(ASCE)ST.1943-541X.0001979
McLain TE (1975) Curvilinear load-slip relations in laterally loaded nailed joints Unpublished doctoral dissertation). Colorado State University, Fort Collins, Colorado
Morris EN (1967) The rotational rigidity of nailed joints in double shear and subjected to short term loading (Research Report E/RR/25). T.R.A.D.A, National Design Specification for Wood Construction, Washington, D.C
Nguyen H (2020) Embedment strength of lvl and cross-banded lvl manufactured from tropical hardwood. Department of Primary Industries, Queensland
Pelletier B, Doudak G (2019) Investigation of the lateral-torsional buckling behaviour of Engineeredwood I-Joistswith varying end conditions. Eng Struct 187:329–340. https://doi.org/10.1016/j.engstruct.2019.03.003
Pellicane PJ, Stone JL, Daniel Vanderbilt M (1991) Generalized model for lateral load slip of nailed joints. J Mater Civ Eng 3(1):60–77
Piazza M, Polastri A, Tomasi R (2011) Ductility of timber joints under static and cyclic loads. Proc Inst Civ Eng Struct Build 164(2):79–90
Porteous J, Kermani A (2013) Structural timber design to Eurocode 5. John Wiley & Sons
prEN 1995-1-1 (2020) Third draft of chapter Connections. 115
Rodd PD (1973) The analysis of timber joints made with circular dowel connectors (Unpublished doctoral dissertation). University of Sussex, England
Schweigler M, Bader TK, Bocquet JF, Lemaître R, Sandhaas C (2019) Embedment test analysis and data in the context of phenomenological modeling for dowelled timber joint design. International Network on Timber Engineering Research (INTER) -Meeting fifty-two, Tacoma (US)(INTER / 52 - 07 - 8), 1–17
Schweigler M, Bader TK, Hochreiner G, Unger G, Eberhardsteiner J (2016) Load-to-grain angle dependence of the embedment behavior of dowel-type fasteners in laminated veneer lumber. Constr Build Mater 126:1020–1033
Schweigler M, Bader TK, Hochreiner G, Unger G, Eberhardsteiner J (2016) Load-to-grain angle dependence of the embedment behavior of dowel-type fasteners in laminated veneer lumber. Construct Build Mater 126:1020–1033
Schänzlin J, Fragiacomo M (2018) Analytical derivation of the effective creep coefficients for timber-concrete composite structures. Eng Struct 172:432–439. https://doi.org/10.1016/j.engstruct.2018.05.056
Sebastian W, Cao C (2024) Hardwood and softwood timber-natural stone composite connections. Constr Build Mater 418:134707
Sjödin J, Serrano E, Enquist B (2008) An experimental and numerical study of the effect of friction in single dowel joints. Holz Roh-Werkst 66(5):363–372
Smith I, Whale L, Anderson C, Hilson B, Rodd P (2011) Design properties of laterally loaded nailed or bolted wood joints. Can J Civ Eng 15(4):633–643
Tomasi R, Crosatti A, Piazza M (2010) Theoretical and experimental analysis of timber-to-timber joints connected with inclined screws. Constr Build Mater 24(9):1560–1571
Wang F, Wang X, Cai W, Chang C, Que Z (2019) Effect of inclined self-tapping screws connecting laminated veneer lumber on the shear resistance. BioResources 14(2):4006–4021
Wang S, Lin J, Wang F, Wang Y, Kong F, Ma P, Que Z (2025) Mechanical behavior and theoretical modeling of wooden nails under various stress conditions. Constr Build Mater 458:139624
Wilkinson TL (1971) Theoretical lateral resistance of nailed joints. J Struct Div 97(5):1381–1398
Wilkinson TL (1972) Analysis of nailed joints with dissimilar members. J Struct Div 98(9):2005–2014
Wilkinson TL (1972) Effect of deformed shanks, prebored lead holes and grain orientation on the elastic bearing constant for laterally loaded nailed joints (Research Paper FPL 192). U.S.D.A, Forest Service, Madison, Wisconsin
Wilkinson TL (1974) Elastic bearing constant of wood: effects of moisture content conditions (Research Paper FPL 235). U.S.D.A. Forest Service, Forest Products Lab, Madison, Wisconsin
Wilkinson TL (1974) Elastic bearing constants for sheathing materials (Research Paper FPL 224). U.S.D.A. Forest Service, Forest Products Lab, Madison, Wisconsin

Xu B, Bouchaïr A, Taazount M, Vega E (2009) Numerical and experimental analyses of multiple-dowel steel-to-timber joints in tension perpendicular to grain. Eng Struct 31:2357–2367

Yeoh D, Fragiacomo M, De Franceschi M, Heng Boon K (2011) State of the art on timber-concrete composite structures: Literature review. J Struct Eng 137(10):1085–1095. https://doi.org/10.1061/(ASCE)ST.1943-541X.0000353

Zhang E, Chen G, Wang C, Zhu W, Yang W (2024) Experimental investigation on lateral performance of southern pine nailed connections under monotonic and cyclic loading. Struct 69:107334

Zhang H, Shen M, Deng Y, Andras P, Sukontasukkul P, Yuen TY et al (2023) A new concept of bio-based prestress technology with experimental proof-of-concept on bamboo-timber composite beams. Constr Build Mater 402:132991

Zhou Y, Cheuk C, Tham L (2009) An embedded bond-slip model for finite element modelling of soil–nail interaction. Comput Geotech 36(6):1090–1097

Zhu W, Yang H, Liu W, Shi B, Ling Z, Tao H (2019) Experimental investigation on innovative connections for timber–concrete composite systems. Constr Build Mater 207:345–356. https://doi.org/10.1016/j.conbuildmat.2019.02.079